Journal of Marine Science and Application (2026) 25: 1332-1348
https://doi.org/10.1007/s11804-025-00756-8

RESEARCH ARTICLE

Burst Pressure Prediction of Corroded Pipes Using Finite Element Analysis–Machine Learning Models Considering Pigging Data: A Case Study of Offshore Pipelines

Sina Kooshamanesh[1], Mohammad Mahdi HajiAbadi[2] and Vahid Salari[3]

Received: 27 March 2025 / Accepted: 04 September 2025
© Harbin Engineering University and Springer-Verlag GmbH Germany, part of Springer Nature 2026

Abstract

Accurate prediction of the burst pressure of corroded pipes is crucial for preventing their failure. This study integrates finite element method (FEM) simulations with machine learning (ML) models to predict the burst pressure with high accuracy. FEM analyses, employing both solid and shell elements, were performed on offshore API 5L X65 steel pipes with real-world multiple corrosion defects. The burst pressure was estimated by applying a factor of 1.05 to the instability criterion. Shell elements yielded results comparable to those of solid elements, while also significantly reducing computational time from 55.82 h to 25.75 h. Three ML models—multilayer perceptron, Gaussian process, and support vector machine—were developed based on three different input groups. Among them, the support vector machine demonstrated the best performance, achieving the highest coefficient of determination (R^2 = 0.95). SHapley Additive exPlanations (SHAP) analysis identifies average defect depth as the most influential parameter, contributing 56.21% to predictions and exhibiting an inverse correlation with burst pressure, aligning with real-world behavior.

Keywords Burst pressure; Finite element method; Machine learning models; Multiple corroded offshore pipes

1 Introduction

Pipelines are a critical component of the transportation infrastructure in the oil and gas industry. Extensive pipeline networks spanning millions of kilometers worldwide serve as an efficient and cost-effective means to meet global energy demands. However, pipelines are susceptible to various types of damage depending on their operating conditions, including wet H_2S exposure (Mucek, 1999), high-temperature hydrogen attack (Poorhaydari, 2019), hydrogen embrittlement (Zvirko et al., 2024), and corrosion (Xing et al., 2024). Among these, corrosion remains a major challenge that causes substantial direct and indirect economic losses. According to the NACE International (formerly, National Association of Corrosion Engineers) (Koch et al., 2016), the global corrosion cost is estimated at US $2.5 trillion annually. A comparative study of corrosion costs across Australia, China, Finland, Germany, India, Japan, Kuwait, the United Kingdom, and the United States revealed that their annual corrosion-related expenses accounted for approximately 1%–5% of their gross national product. Given these economic implications, pipeline integrity assessment plays an important role in preventing unexpected leaks or ruptures.

The conventional approach to assessing corroded pipelines is based on code-based standards, such as ASME B31G (2012) and DNV-RP-F101 (2019). Although these standards offer reliable assessment methodologies, they have some limitations. ASME B31G often yields conservative predictions (Gao et al., 2010), whereas DNV-RP-F101 (2019) recommends that if the spacing between corrosion defects is within $2.5\sqrt{(DT)}$ (where D and T denote the pipeline diameter and wall thickness, respectively), they should be considered to be interacting; otherwise, they can

Article Highlights

- 128 real-world multiple corroded API 5L X65 offshore pipes were analyzed by finite element method.
- The burst pressure was predicted using machine learning methods.
- The most accurate prediction was achieved using the number of defects, average defect length, and average defect depth as input features.
- According to feature importance and SHapley Additive exPlanations (SHAP) analysis, average defect depth was the greatest impact on burst pressure, with an inverse relationship.

✉ Sina Kooshamanesh
sina.kooshamanesh@modares.ac.ir

[1] Department of Materials Engineering, Tarbiat Modares University, Tehran 14115-143, Iran

[2] School of Electrical Engineering, University of Guilan, Rasht 4199613776, Iran

[3] Department of Materials and Metallurgical Engineering, Ferdowsi University of Mashhad, Mashhad 9177948974, Iran

be analyzed independently. Despite their utility, code-based methods tend to be overly conservative and fail to accurately represent the actual operational conditions of corroded pipes. Furthermore, these methods depend on material toughness. To minimize subjectivity and incorporate uncertainty, Bhardwaj et al. (2022) devised a method for evaluating the dependability of corroded pipes using calibrated strength models. They evaluated the efficacy of 25 burst strength models against test data, classifying them by steel grade (low, medium, and high). The first-order reliability method was employed for reliability and sensitivity assessments. This approach was considered an improvement over existing methods because it utilized accurate strength models and accounted for model uncertainties. In a subsequent study, a probabilistic framework was presented that utilized hierarchical Bayesian analysis to calibrate burst strength models for uncorroded and corroded pipelines. They determined model uncertainty factors for calibration and grouped prediction models according to steel grade. For uncorroded and corroded pipelines across the three material groups, their findings included estimated mean values and uncertainty of posterior probabilities for model uncertainty factors. Additionally, they discovered that as the severity of corrosion defects increased, the prediction uncertainties tended to grow nonlinearly. The importance of this method was demonstrated in a case study that showed variations in uncertainty compared to the traditional methods. Furthermore, hierarchical Bayesian-based regression analysis was used to construct model uncertainty factors for corroded pipes as a function of defect depth. Finally, the calibrated models yielded nonconservative forecasts (Bhardwaj et al., 2024). Amaya-Gómez et al. (2019) demonstrated that models such as DNV-RP-F101 (2019), CPS (Cronin and Pick, 2002) and CUP (Shuai et al., 2017) are suitable for studying low-toughness materials. Models suitable for moderate-toughness materials include PCORRC (Stephens and Leis 2016) and those reported by Ma et al. (2013), Netto et al. (2005), and Zhu and Leis (2005), whereas for high-toughness materials, PCORRC and the models reported by Chen et al. (2015), Ma et al. (2013), and Choi et al. (2003) provide overall remarkable results. Adib-Ramezani et al. (2006) examined the structural integrity of externally corroded X52 gas pipes with three distinct defect types: semispherical, semielliptical, and blunt notch. Their findings revealed that the safety factor for blunt notch defects could only be calculated using SINTAP levels 0 B and 1 B (Webster and Bannister 2000), as these were the only standards that incorporated empirical equations for such defects. Furthermore, Adib-Ramezani et al. (2006) established that DNV-RP F-101 and Choi et al. (2003) defined the upper and lower limits of the safety factor for both semispherical and semielliptical defects.

To overcome the limitations of code-based standards, the finite element method (FEM) has been widely utilized to obtain highly accurate assessments or to focus on improving code-based standards by considering different aspects, such as material or corrosion geometry. Alang et al. (2013) compared burst pressure predictions using FEM, ASME B31G, modified ASME B31G, and DNV-RP-F101 (2019) and reported that FEM provided the highest burst pressure values, while ASME B31G was the most conservative. To reduce the conservatism of DNV-RP-F101 (2019), Arumugam et al. (2020) developed six predictive equations using FEM for internally and externally corroded pipes; these equations incorporate the von Mises and Tresca criteria. Their analytical model, validated through FEM, yielded higher accuracy than the conventional methods.

Owing to the complexities involved in accurately modeling defects, simplifications are often applied; for example, the assumption of rectangular defect shapes. Karuppanan et al. (2014) demonstrated that incorporating fillets at the edges of rectangular defects increased the burst pressure value by 3.5%. Meanwhile, Yu et al. (2011) reported a 4.5% difference in bending moments between rigid and smooth-edged (fillet) defects.

The FEM-based burst pressure analysis is not limited to single-corroded areas; the method also accounts for multiple interacting defects. The interaction of defects results in a reduction in failure pressure (Chen and Shu, 2001). Sun and Cheng (2018) performed FEM simulations on pipelines with overlapping and divided circumferential and longitudinal defects, concluding that defect interaction is significant only within a specific distance. This threshold was defined as the ratio of the failure pressure of multiple corrosion defects to that of a single defect. Defect interaction was observed when this ratio was below 0.99. Additionally, interaction effects were more pronounced in the circumferential direction than in the longitudinal direction. For overlapping defects, stress concentration in the lower defect led to a failure pressure much smaller than that in single-corroded pipes. Zhou et al. (2022) further identified that the depth of the deepest defect was the most critical factor, followed by defect length and axial distance between defect clusters.

The abundance of information over the last decade has emphasized the effectiveness of data-driven methods such as machine learning (ML). Zhang et al. (2024) demonstrated that an optimized XGBoost model predicted burst pressure much more accurately than conventional code-based standards; feature importance analysis identified pipe thickness and corrosion length as the most influential factors. Abyani et al. (2022) utilized six ML models and confirmed that wall thickness and corrosion defects significantly affected the failure pressure of single-corroded pipes. Their study also revealed an inverse relationship between the water depth and internal pressure from the viewpoint of the maximum von Mises stress (MVMS). Specifically, at

low internal pressure, an increase in water depth led to a higher MVMS, whereas at greater depths, an increase in internal pressure resulted in a lower MVMS. Cai et al. (2022) explored the use of data-driven ML methods to predict the burst strength of corroded line pipelines subjected to internal pressure, offering an alternative to the traditional, more limited approaches. They utilized three supervised ML algorithms: the artificial neural network (ANN), support vector machine (SVM), and linear regression (LR). These models were trained on a dataset of 115 experimental pipe burst tests, gathered from previous papers, focusing on cases with a single corrosion defect. Although some data points were machined, meaning that they had a rectangular shape (Mok et al., 1991; Benjamin et al., 2000; Choi et al., 2003; Freire et al., 2006), the others were natural type, meaning that they had an irregular shape, and only the maximum depths of defects were reported in the literature (Cronin et al., 1996; Cronin and Pick, 2000). While the ANN model with three neural layers achieved the highest training accuracy (0.969), it also showed the largest variance, indicating overfitting. In contrast, the SVM model demonstrated both high training and validation accuracy. The LR model provided the best performance in terms of generalization ability among the proposed models. Cai et al. (2022) suggested these models can serve as valuable surrogate models for future transfer learning applications, aiding in sustainable and intelligent decision-making for ensuring pipeline integrity. Jiang and Dong (2024) developed a method that combines random fields, convolutional neural networks (CNNs), and FEM to predict the residual strength when both random and isolated external corrosion defects are present. By modeling corrosion morphologies using symmetric finite element models with a solid mesh, their CNN model achieved robust performance while reducing computational costs by more than 30 000 times. Additionally, Abyani et al. (2024) integrated FEM with ANNs to enhance failure predictions for pipelines with a single external corrosion defect, outperforming code-based standards. While the FEM results for medium and small defects were close to these standards, the predictions for large defects showed strong agreement with ASME B31G calculations. Similarly, Liu et al. (2020) conducted a parametric analysis to predict the failure pressure of pipes with a single external corrosion defect by integrating FEM with ANNs by using the ratio of pipe diameter to wall thickness, nondimensional corrosion defect length, and defect depth as input variables. They found that the maximum observed error between the ANNs and experimental results was 16%.

While numerous studies explored the integration of FEM and ML models, a key limitation remains: research has mainly focused on the combination of FEM and ML in single-defect case studies or the application of only ML models to experimental single-defect scenarios (Abyani et al., 2022, 2024; Cai et al., 2022; Zhang et al., 2024). These studies typically assumed isolated damage zones, which may not accurately represent the complex conditions encountered in real pipeline systems. However, in actual operating environments, corrosion defects often appear in clusters, varying significantly in size, depth, and spacing. These defects can interact, forming stress concentration zones and nonlinear failure behaviors that drastically affect burst pressure. This interaction complicates the prediction process and introduces additional uncertainties that have been rarely addressed in the existing ML-FEM models. Furthermore, studies regarding multiple defect corrosion are mostly limited to FEM-based approaches (Sun and Cheng, 2018; Zhou et al., 2022), which do not incorporate ML to generalize patterns or improve prediction efficiency. Hence, there appears to be a gap in the current literature regarding the combined use of FEM and ML to address the interactions among multiple corrosion defects. This study aims to contribute toward filling this gap by developing a framework that incorporates both approaches under more realistic defect conditions. To address this gap and to understand the capability of ML models to predict the burst pressure in real scenarios, finite element analyses were performed using both shell and solid elements on API 5L X65 steel offshore pipes containing multiple corrosion defects. The accuracy and efficiency of the results obtained using the two elements were compared. Burst pressure calculations were conducted as per the API 579 instability criteria, with subsequent refinements using the DNV-RP-F101 (2019) procedure. Furthermore, three ML models, including multilayer perceptron (MLP), Gaussian process (GP), and SVM, were developed based on three distinct input approaches to predict burst pressure. The most accurate model was identified through statistical evaluation. The SHapley Additive exPlanations (SHAP) analysis was performed for this model to determine the contribution and influence of each input parameter on burst pressure predictions.

2 Method

2.1 FEM procedure

In this study, pipes with an outer diameter of 812.6 mm and a nominal thickness of 20.6 mm were modeled using ABAQUS software. Since the shape of defects drastically influences stress analysis, defects were identified through pigging. Figure 1 shows the rectangular defects observed in one of the examined pipes. Solid elements were used in previous single-defect studies (Arumugam et al., 2020; Abyani et al., 2022); however, using shell elements reduces analysis costs in multiple-defect cases. Therefore, to assess the effectiveness of shell elements, six models were analyzed separately using solid and shell elements. Then, the burst

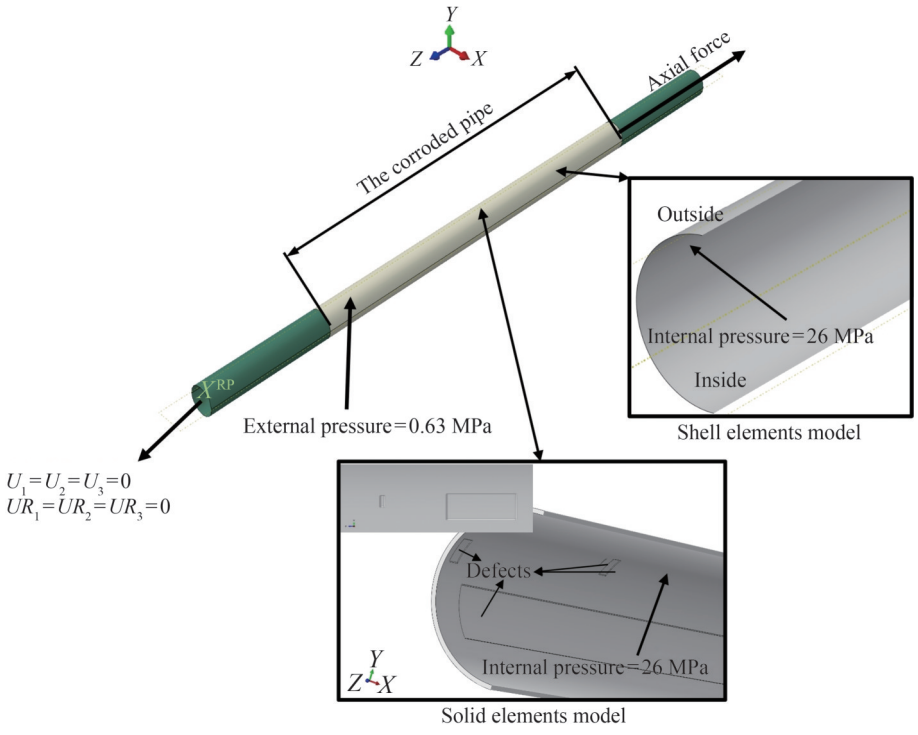


Figure 1 Configuration of the finite element model, including the boundary conditions, loads, and an overview from inside the finite element models with both shell and solid elements

pressure predictions from both approaches were compared to select the most appropriate approach. As shown in Figure 1, defects can be seen in the preprocessing of the solid element model, while in the shell element model, no defect areas can be observed. This is because thickness values were assigned by the mapped field technique (ABAQUS, 2022) in the shell element approach. This technique allows us to define spatially varying parameter values from an external data source based on four variables: x, y, z, and the field value. In this study, x, y, and z represent the coordinates of each node in the shell element approach, while the field value represents thickness. The thickness value at each node was implemented using an in-house MATLAB code. Figure 2 provides the typical details of one of the corroded pipes analyzed in this study. Specifically, Figure 2(a) shows the actual corroded areas determined based on pigging data. Additionally, Figure 2(b–d) show the distributions of three key parameters extracted from the pigging data provided in Figure 2(a): circumferential length of defects, depth of defects and longitudinal length of defects, respectively. Figure 2(e) shows the thickness map generated using the in-house MATLAB code.

As shown in Figure 2(a), the corrosion defects detected by the pigging device were longitudinally aligned with the pipe axis (corrosion angle = 0°). The device segmented the corrosion zones into rectangular profiles. The maximum depth observed within each zone was reported as a uniform value across the entire area. This limitation arises from the pigging software itself. Consequently, the defect shapes were modeled in the finite element model based on these simplifications. According to Figure 1, two additional sections, each with a length equal to five times the outside diameter, were included in the models to apply boundary conditions.

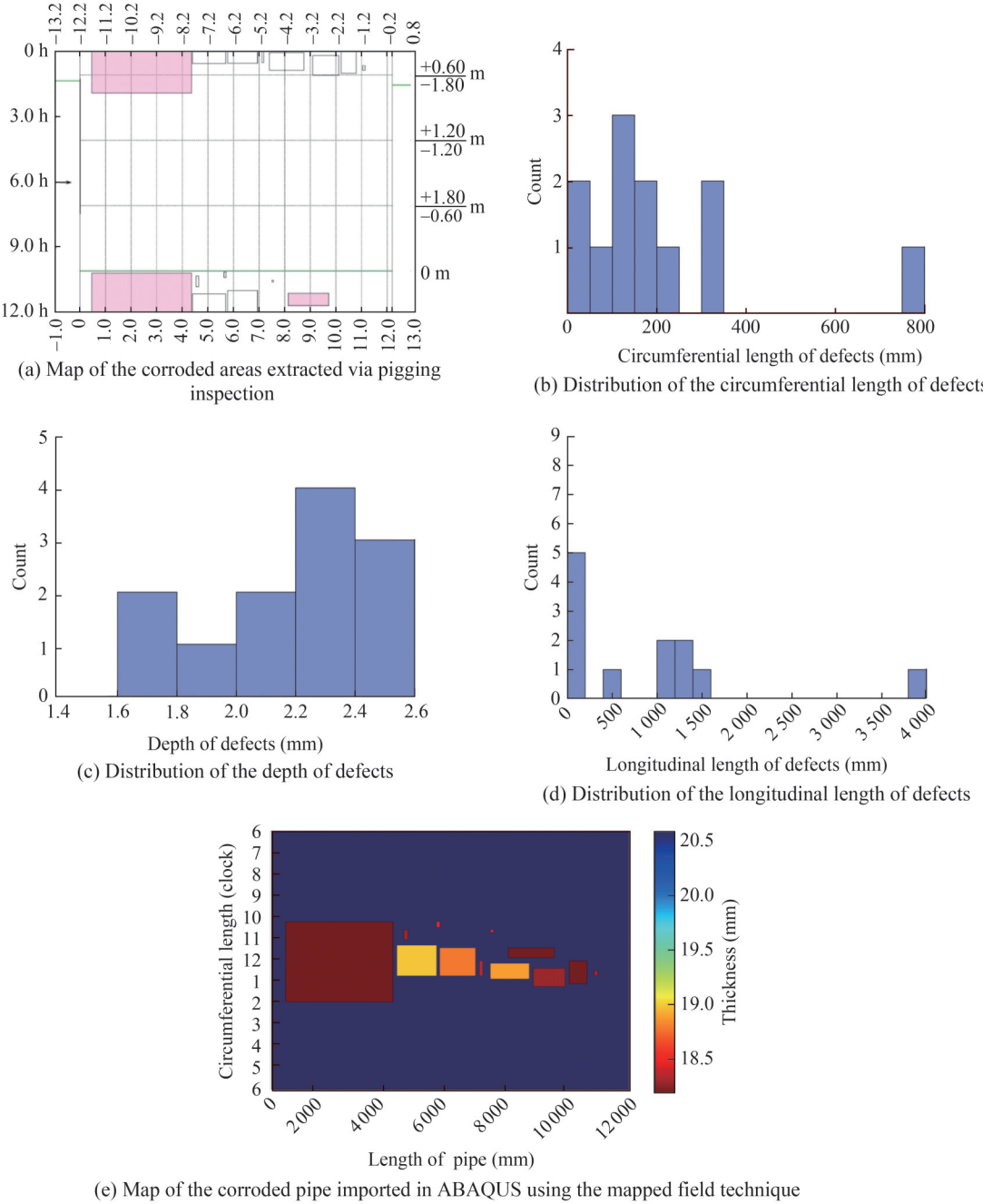
Both boundary conditions and loads are shown in Figure 1. The boundary conditions were defined to model an infinite pipeline (Fallqvist, 2009; Barbosa et al., 2017). The pipe was assumed to be straight and fully supported by the seabed, without any free span. To achieve this, one end of the pipe was coupled with a reference point, allowing unrestricted radial expansion. The reference point was fixed, while the opposite end was left free to expand.

In each model, three loads were considered based on a real-world scenario: the external pressure (P_e), which originates from the hydrostatic effect of the seawater and is equal to 0.63 MPa; the internal pressure (P_i), which arises from the transported fluid, and the value of the maximum allowable working pressure is 26 MPa for an intact pipe; and the axial force, which is calculated to be 46 kN using Eq. (1) (DNV-ST-F101 2017):

$$S = N - P_i A_i + P_e A_e \tag{1}$$

where N represents the axial force in the pipe wall, A_i denotes the internal cross-sectional area, and A_e is the external cross-sectional area.

All pipes were fabricated from API 5L X65 and analyzed using nonlinear elastic–plastic finite element analysis



(a) Map of the corroded areas extracted via pigging inspection

(b) Distribution of the circumferential length of defects

(c) Distribution of the depth of defects

(d) Distribution of the longitudinal length of defects

(e) Map of the corroded pipe imported in ABAQUS using the mapped field technique

Figure 2 Pigging inspection data including the corrosion map, statistical information on defect dimensions, and the corrosion map imported into ABAQUS using the mapped-field technique

(FEA). The true stress–strain relationship was derived using the MPC project (API 579 2019), as described in Eqs. (2)–(12), where σ_t represents true stress; σ_{ys} is the yield stress; σ_{uts} denotes the engineering ultimate tensile strength; ε_p is the true plastic strain; ε_{ys} represents the engineering offset strain; and E_y is Young's modulus. Moreover, all material constants, including m_1, m_2, A_1, and A_2, at a service temperature of 63 °C, as well as the true stress–strain relationship, are shown in Figure 3. The Young's modulus and Poisson's ratio were taken as 207 GPa and 0.3, respectively.

$$\varepsilon_t = \frac{\sigma_t}{E_y} + \gamma_1 + \gamma_2 \tag{2}$$

$$\gamma_1 = \frac{\varepsilon_1}{2}\left(1.0 - \tanh\left[H\right]\right) \tag{3}$$

$$\gamma_2 = \frac{\varepsilon_2}{2}\left(1.0 - \tanh\left[H\right]\right) \tag{4}$$

$$\varepsilon_1 = \left(\frac{\sigma_t}{A_1}\right)^{\frac{1}{m_1}} \tag{5}$$

$$A_1 = \frac{\sigma_{ys}(1+\varepsilon_{ys})}{\left(\ln\left[1+\varepsilon_{ys}\right]\right)^{m_1}} \tag{6}$$

$$m_1 = \frac{\ln[R] + (\varepsilon_p - \varepsilon_{ys})}{\ln\left[\frac{\ln[1+\varepsilon_p]}{\ln[1+\varepsilon_{ys}]}\right]} \tag{7}$$

$$\varepsilon_2 = \left(\frac{\sigma_t}{A_2}\right)^{\frac{1}{m_2}} \tag{8}$$

$$A_2 = \frac{\sigma_{uts}\exp[m_2]}{{m_2}^{m_2}} \tag{9}$$

$$H = \frac{2\left[\sigma_t - \left(\sigma_{ys} + K\left(\sigma_{uts} - \sigma_{ys}\right)\right)\right]}{K\left(\sigma_{uts} - \sigma_{ys}\right)} \tag{10}$$

$$R = \frac{\sigma_{ys}}{\sigma_{uts}} \tag{11}$$

$$K = 1.5R^{1.5} - 0.5R^{2.5} - R^{3.5} \tag{12}$$

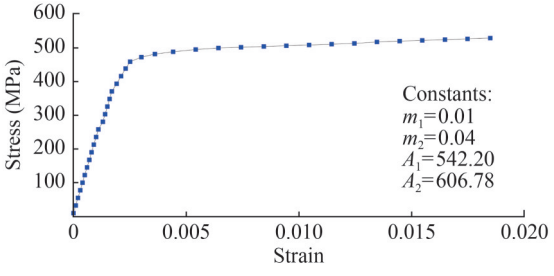


Figure 3 True stress–strain curve for API 5L X65 based on MPC

The stress analysis of corroded pipes was conducted using both solid and shell element methods. C3D8R elements were utilized for the solid element approach, and S4R elements for the shell element approach. The failure criterion was defined as the pressure causing instability and was identified as the last pressure before divergence. It is commonly referred to as the burst pressure of the finite element (Mokhtari and Melchers, 2018; Zangeneh, 2021).

According to DNVGL-ST-F101 (2017), the design resistance (R_{Rd}) incorporates two factors, γ_m and γ_{SC}, which are taken as 1.15 and 1.138, respectively, resulting in a combined factor of $\gamma_m \times \gamma_{SC} = 1.31$ for a medium safety class. Furthermore, according to this standard, the usage factor applied in determining the safe working pressure has two components: the modeling factor, $F_1 = 0.9$, and the operational usage factor, F_2, introduced to ensure a sufficient safety margin between the operating pressure and the failure pressure of the corrosion defect. F_2 is typically equal to the design factor. The total usage factor (F) is calculated as $F = F_1 \times F_2$, yielding $F = 0.9 \times 0.74 = 0.67$. Consequently, as per paragraph G.2.5 of BS 7910: 2019, the minimum factor of safety is 1.5.

The FEM procedures for solid and shell elements are shown in Figure 4. For the shell element model, uncorroded pipes were initially generated. Subsequently, thickness values were assigned using the mapped field technique through an in-house MATLAB program. The instability pressure and safe working pressure were calculated in accordance with the DNV-RP-F101 (2019) criterion. According to this standard, the rectangular assumption typically results in conservative predictions of the load-carrying capacity because of exaggeration of the effective defect area. To account for this problem, the standard introduces a correction factor of 1.05. This factor was applied when calculating the safe working pressure. For the solid element model, most of the steps are the same as those for the shell elements. However, the corroded pipes in the solid element model are generated by removing the corroded areas instead of by modifying the thickness values. The data of each model were recorded for performing burst pressure predictions using ML models

2.2 Machine learning procedure

Although the FEM is a powerful tool for assessing the integrity of industrial components, it requires considerable computational resources. In this situation, data-driven methods such as ML models provide an efficient alternative for predicting burst pressure. This study aimed to develop a reliable method for predicting burst pressure based on failure criteria. The overall procedure is illustrated in Figure 5.

Alang et al. (2013) found that the depth of defects is the most influential factor for burst pressure. Ma et al. (2013) showed that the width of defects has minimal effect on burst pressure. As shown in Figure 2(e), the pipes considered in this study contain multiple defects. Since prior literature focused on pipes containing a single defect (Abyani et al., 2022, 2024; Cai et al., 2022; Zhang et al., 2024), it was necessary to define appropriate parameters to reflect the condition of the pipes in this study. Therefore, the representative values for defect depth and length were determined by calculating their average values (d_{avg} and L_{avg}), respectively, based on studies on additive manufacturing (Luo et al., 2022) and fatigue (Beretta, 2021). However, unlike previous studies that did not include the number of defects ($N_{defects}$) as an input, this study included $N_{defects}$ because it was different for each pipe. Additionally, three volumetric variables, including the average volume of defects (V_{avg}), minimum volume of defects (V_{min}), and maximum volume of defects (V_{max}), were derived to investigate the interactions between defect dimensions (depth, width, and

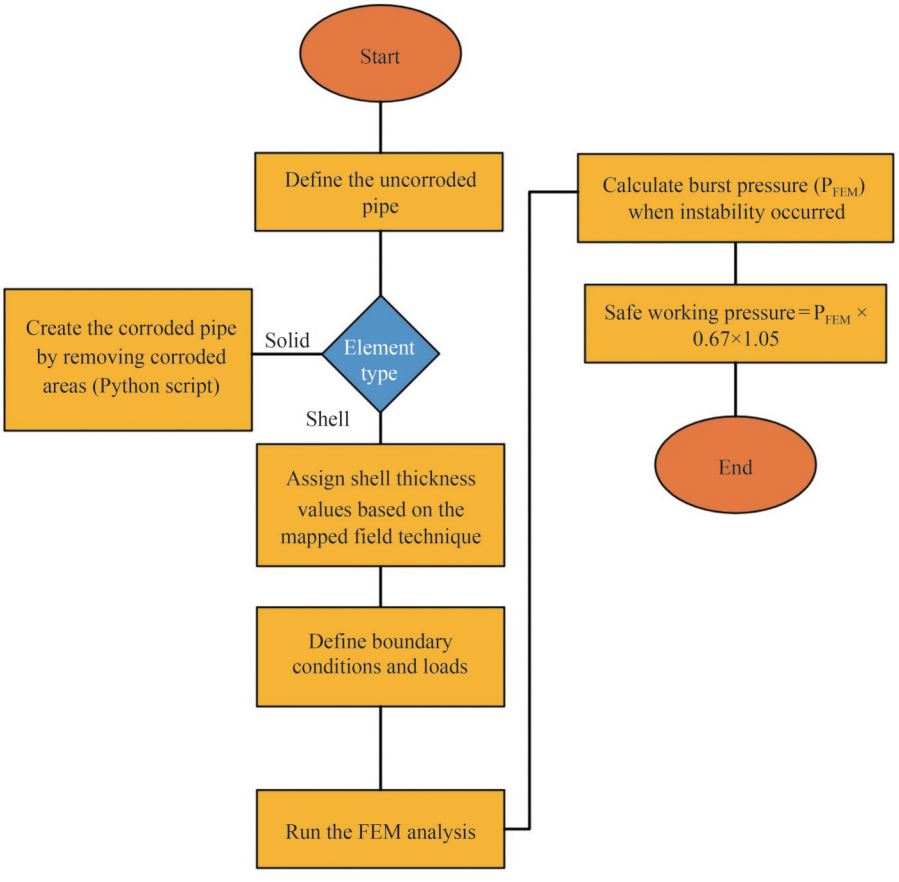


Figure 4 Finite element modeling flowchart used in this study

length)—this approach is similar to the approach adopted by Du et al. (2017) for analyzing the failure mode of pressure vessels containing volumetric defects. Notably, inputs to ML models must be independent; hence, three groups of inputs were defined in this investigation. In Group 1, the $N_{defects}$ and V_{avg} were used as input variables. In Group 2, $N_{defects}$, L_{avg}, and d_{avg} were considered as inputs. In Group 3, $N_{defects}$, V_{min}, and V_{max} were used as input parameters. In all three groups, the safe working pressure was the output variable. The inner and outer radii of the pipes were considered constant, with values of 406.4 and 385.8 mm, respectively. Additionally, the pipe length was kept constant at 12 m in all cases. Figure 6 provides the distribution of all inputs. The distributions of $N_{defects}$, L_{avg}, V_{avg}, V_{max}, and V_{min} are skewed. Hence, to obtain a distribution similar to a normal distribution, all inputs were transformed using quantile transformation.

Three algorithms were implemented in this study to develop the ML models. ANNs consist of multiple layers of interconnected artificial neurons that mimic the neural network structure of the human brain. Neurons are connected via multiple communication pathways, with each neuron functioning as an independent computing unit. This enables ANNs to perform complex computations. ANNs are an important tool for engineers and researchers to predict critical parameters and make necessary adjustments to optimize results (Ghari et al., 2024). The ANN used in this study was the MLP. The SVM is a form of supervised learning technique designed for high-dimensional feature spaces. By identifying the optimal hyperplane with the largest margin, the SVM effectively classifies data and makes accurate predictions (Hasni et al., 2017). The GP is a nonparametric kernel-based method that operates within a Bayesian framework and uses statistical principles to establish a mapping relationship between the dependent and independent variables (Wang et al., 2021).

To ensure optimal performance of the ML models, hyperparameter tuning was performed using a grid search strategy across nine conditions (three ML models across three groups), as listed in Table 1. The dataset contained 128 data points, which were randomly divided into training and test sets with a ratio of 70 (89 data points):30 (39 data points).

Activation functions play a critical role in training neural networks as these functions introduce nonlinearity, allowing the network to capture complex relationships. Two widely used activation functions are the hyperbolic tangent function (tanh) and the logistic function (sigmoid). Both functions have similar structures; however, the hyperbolic tangent function ranges between −1 and 1, while the

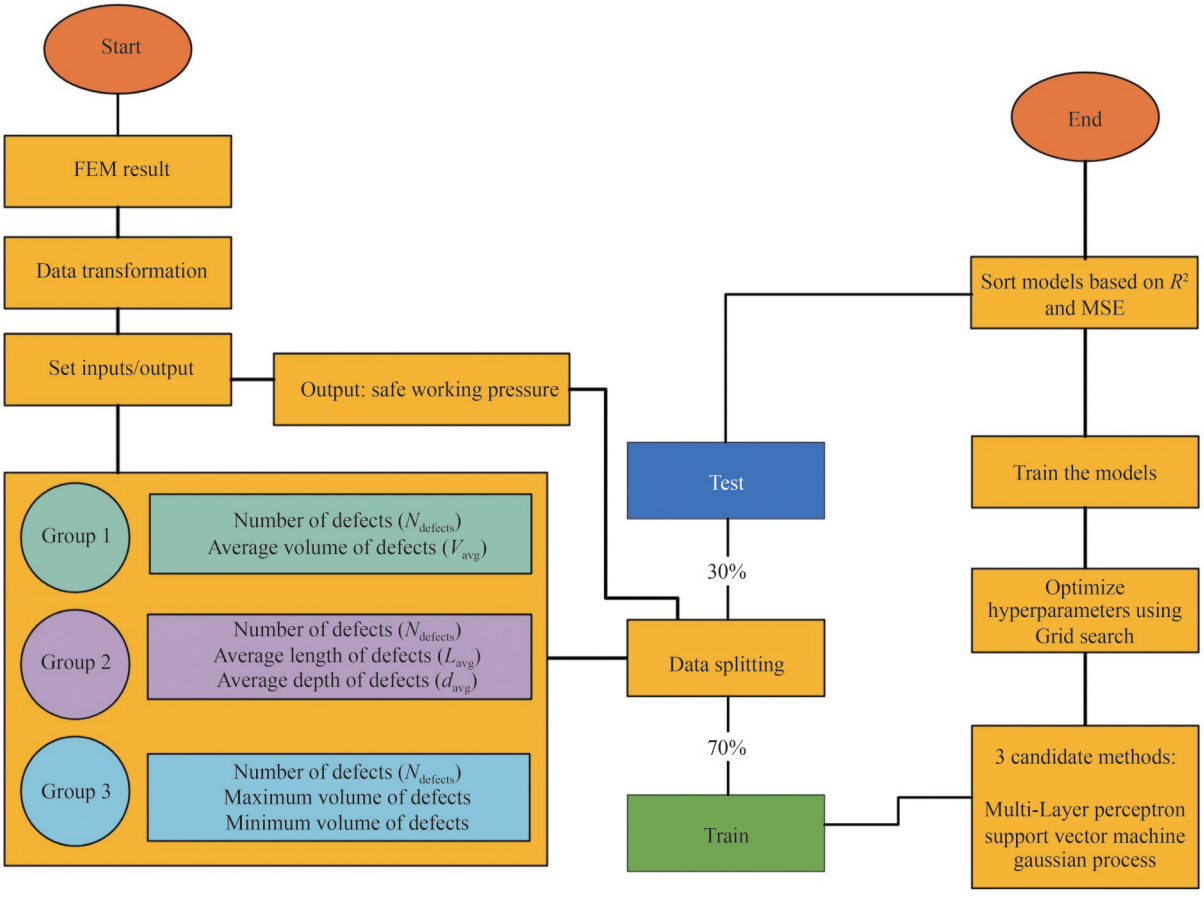


Figure 5 Machine learning (ML) modeling procedure employed in this study

logistic function ranges between 0 and 1. These functions are mathematically defined as shown in Eqs. (13) and (14) (Rasamoelina et al. 2020).

$$\tanh(x) = \frac{2}{1 + e^{-2X}} - 1 \tag{13}$$

$$\text{standard logistic} = \frac{1}{1 + e^{-X}} \tag{14}$$

where X represents the input values. L-BFGS is a solver that can be applied to small datasets. The second-order partial derivatives of a function are represented by a Hessian matrix, which is approximated by this solver. Furthermore, this solver approximates the inverse of the Hessian matrix to perform parameter updates. The number of neurons affects the complexity of ML models: increasing the number of neurons not only increases the computational time but also leads to overfitting. Conversely, although reducing the number of neurons can reduce computational time, it causes underfitting (Neural network models (supervised)).

The radial basis function (RBF) is a kernel that is commonly used in SVM problems. The RBF is expressed as shown in Eq. (15) (Han et al. 2012).

$$K(x_i, x_j) = \exp\left(-\gamma \left\| x_i - x_j \right\|\right)^2 \tag{15}$$

where x_i and x_j are two input vectors, and γ is an adjustable constant. The extent of influence of a single training sample on SVM is determined by the gamma parameter; a low gamma value implies far-reaching influence, and a large value indicates close influence. The model is very sensitive to gamma—if the factor is too large, each support vector only influences itself, resulting in overfitting; if it is too small, it reduces to a linear model that divides dense areas into various classes. The C parameter achieves the tradeoff between the correct classification of training instances and the maximization of the margin of the decision function. A narrower margin is allowed for greater values of C if the decision function performs better at accurately classifying every training point. A lower C results in a simpler decision function and a wider margin, but at the expense of training accuracy (RBF SVM parameters).

In the context of GP, the alpha value is added to the diagonal of the kernel matrix during fitting to guarantee numerical stability by making the matrix positive definite. Its default value is 1E−10. Additionally, alpha can depict the Gaussian noise variance of the training data (GaussianProcessRegressor).

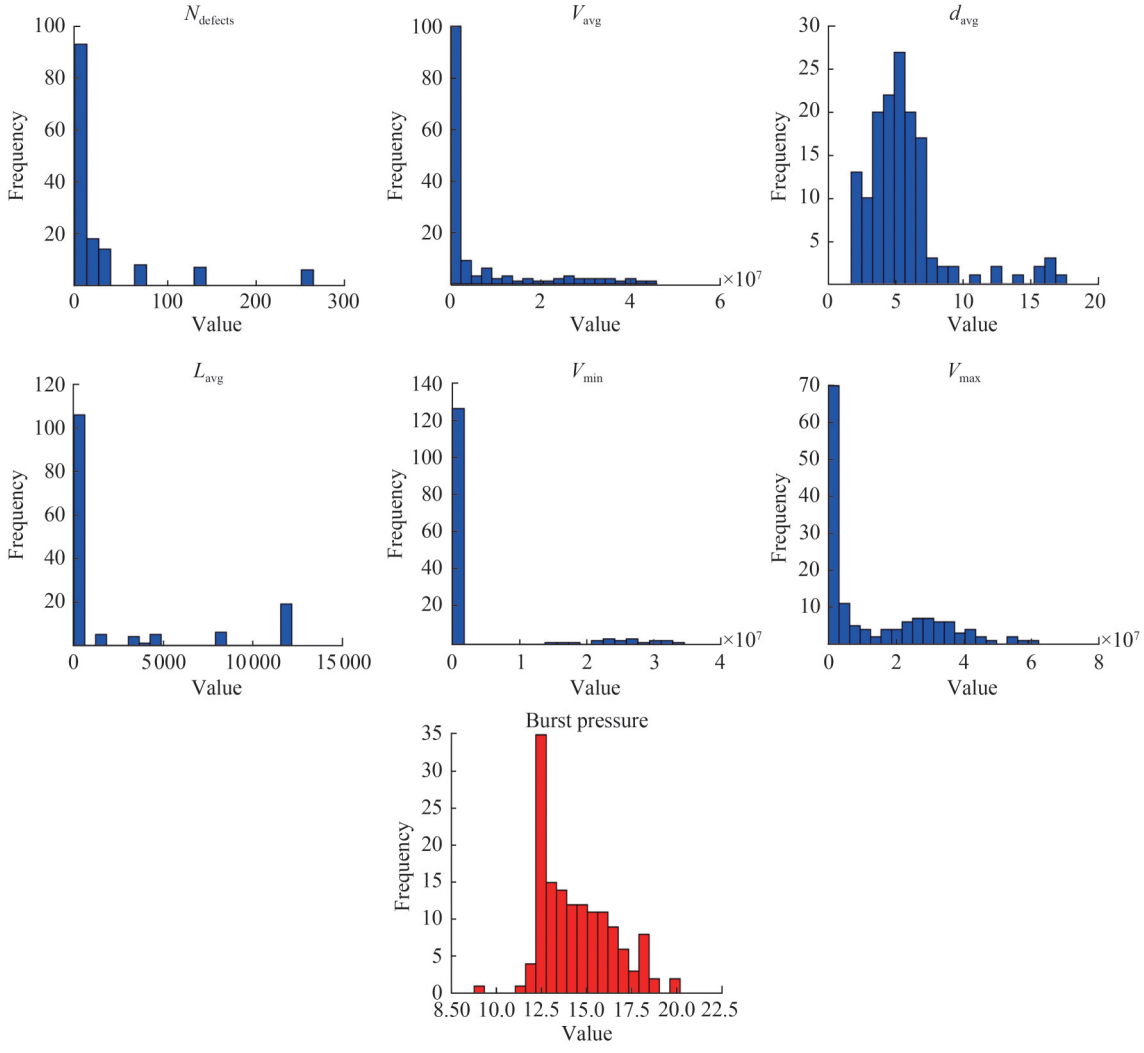


Figure 6 Distribution of all variables: Blue bar charts indicate inputs, while the red bar chart indicates the output

Two statistical criteria were used to evaluate the performance of each ML model under different conditions. The coefficient of determination (R^2) score was used to assess the accuracy of the model for training and test data. It is defined as shown in Eq. (16):

$$R^2 = 1 - \frac{\text{RSS}}{\text{TSS}} \tag{16}$$

where RSS is the sum of squares of residuals, and TSS is the total sum of squares. Additionally, the mean squared error (MSE) was used as a loss function to quantify the difference between the predicted and actual values, as defined in Eq. (17):

$$\text{MSE} = \frac{1}{n}\sum_{i=1}^{n}\left(Y_i - \hat{Y}_i\right)^2 \tag{17}$$

where Y_i represents the actual values, and $\hat{Y}_i$ represents the predicted values.

3 Results and discussion

3.1 Validation

To validate the FEA procedure used in this study, the numerically obtained results were compared with the results for a locally corroded pipe investigated by Yamaguchi (2014). The validation process involved reproducing the numerical findings to ensure accuracy. Figure 7(a) shows the stress distribution and thickness profile of the corroded pipe, demonstrating that the von Mises stress reached the ultimate tensile strength in the corroded area, as shown in Figure 7(b).

Furthermore, Figure 7(c) shows the plots of pressure against increment and increment size against increment. Although the increment size increased to 0.17 s before the 10 th increment, it decreased rapidly thereafter so that during the numerical solution, the increment size was close to 0. In contrast, as the number of increments increased, the pres-

Table 1 Hyperparameters for each condition

Group	ML model	Hyperparameters	Code name
1	MLP	Activation = Logistic Hidden layer size = 52 Learning rate initiation = 0.001 Solver = lbfgs	MLP-1
	SVM	C = 90 $\gamma = 1$ Kernel = RBF	SVM-1
	GP	$\alpha = 10^{-9}$ Normalize y = True Kernel = RBF	GP-1
2	MLP	Activation = tanh Hidden layer size = 20 Learning rate initiation = 0.001 Solver = lbfgs	MLP-2
	SVM	C = 130 $\gamma = 0.1$ Kernel = RBF	SVM-2
	GP	$\alpha = 10^{-7}$ Kernel = RBF	GP-2
3	MLP	Activation = tanh Hidden layer size = 45 Learning rate initiation = 0.001 Solver = lbfgs	MLP-3
	SVM	C = 160 $\gamma = 10$ Kernel = RBF	SVM-3
	GP	$\alpha = 10^{-6}$ Kernel = RBF	GP-3

sure never exceeded 28.5 MPa. According to the API579 procedure, a constant load during the analysis and an increment close to 0 indicate that the analysis does not converge. Therefore, the burst pressure was taken as 28.5 MPa. To assess the validity of this result, the obtained burst pressure was compared with that of Yamaguchi's model (2014). The comparison revealed strong agreement between the two models—the burst pressures in the regenerated and Yamaguchi models were 28.5 and 29 MPa, respectively. This close correlation confirms the accuracy and reliability of the proposed FEA approach.

3.2 Shell and solid models

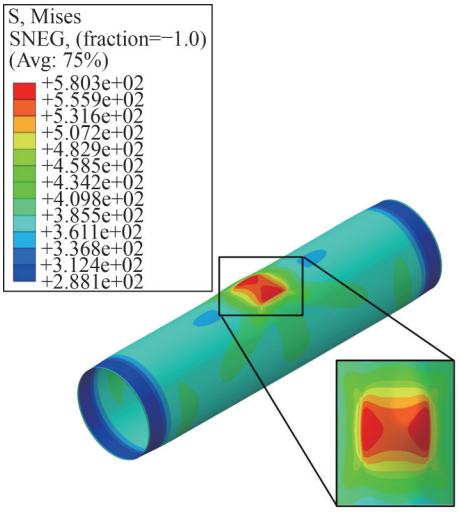
The P6 Shell model with three distinct element sizes, including 20, 10, and 8 mm, was subjected to mesh sensitivity tests to determine the appropriate mesh size for the analyses. A node at the center of the pipe was used to illustrate the changes in displacement. The axial displacement curves for models with 10 and 8 mm element sizes roughly overlapped, as shown in Figure 8(a). Consequently, elements measuring 10 mm were considered sufficient to provide the necessary level of accuracy in the analyses. Moreover, the axial displacement curve for the solid element approach, with a mesh size of 10 mm, shows a trend similar to the shell element approach, which also has a mesh size of 10 mm. Hence, the mesh size for the P6 solid model was chosen to be 10 mm. Figure 8(b) shows a comparison of burst pressures for six pipes modeled using both solid and shell elements. The results indicated that there were no significant differences in the safe working pressure between the two element types. However, the total running time for each model, as shown in Figure 8(c), highlights a key advantage of using shell elements: specifically, the running time for the solid element models (55.82) was approximately twice that of the shell element models (25.75), demonstrating the computational efficiency of the latter models.

The primary reason for the reduced computational cost of shell elements is shown in Figure 8(d). The number of nodes in solid models was at least three times that in the shell models. Figure 9(a) and (b) show the von Mises stress contours for the solid element model of the P6 and the shell element model, respectively. Only a slight difference can be observed between the two models, indicating that both element types provide comparable stress distributions. This demonstrates that the mapped field technique effectively incorporates real thickness variations into the finite element model, ensuring an accurate representation of corrosion defects. Furthermore, a comparison of the real thickness data map (heat map), STH contour values of the shell element model, and defects in the solid element model (white pipe) in Figure 9(c) reaffirmed that the real thickness data can be reliably captured by FEA using the mapped field method. Thus, this approach was validated for modeling corroded pipes. Figure 9(d) shows the thickness and von Mises stress values along path A, which is drawn circumferentially. This figure shows that a decrease in thickness leads to an increase in von Mises stress values. Moreover, the peak von Mises stress is observed at the edges of the defect because of stress concentration.

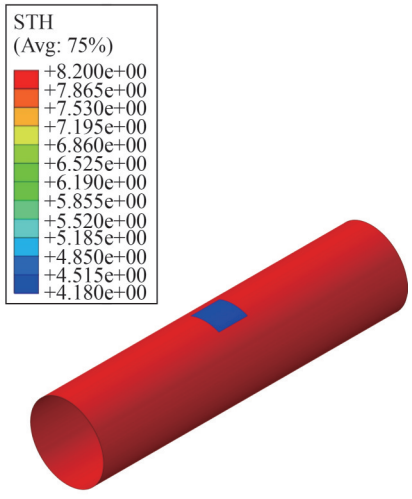
3.3 ML models

Although shell elements are an efficient tool for predicting the burst pressure of multiple corroded pipes, the process is still time-consuming. Hence, this study introduces ML models as an alternative approach for predicting the burst pressure of multiple corroded pipes. The performance of the models is summarized in Table 2.

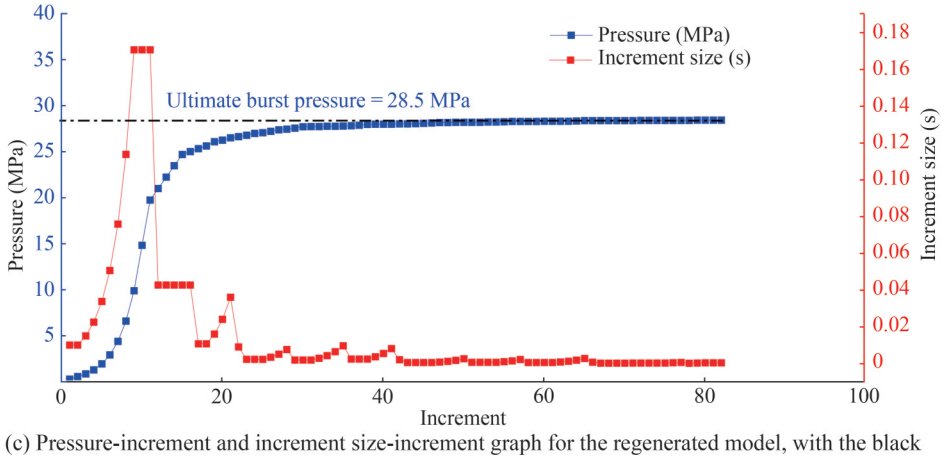
Each model was evaluated based on statistical criteria. The evaluation demonstrated that all models were adequately trained. A comparison of the R^2 values for the training and test sets demonstrated that the features of Group 2



(a) Stress distribution of the regenerated model from isometric and front views



(b) Thickness profile of the regenerated model

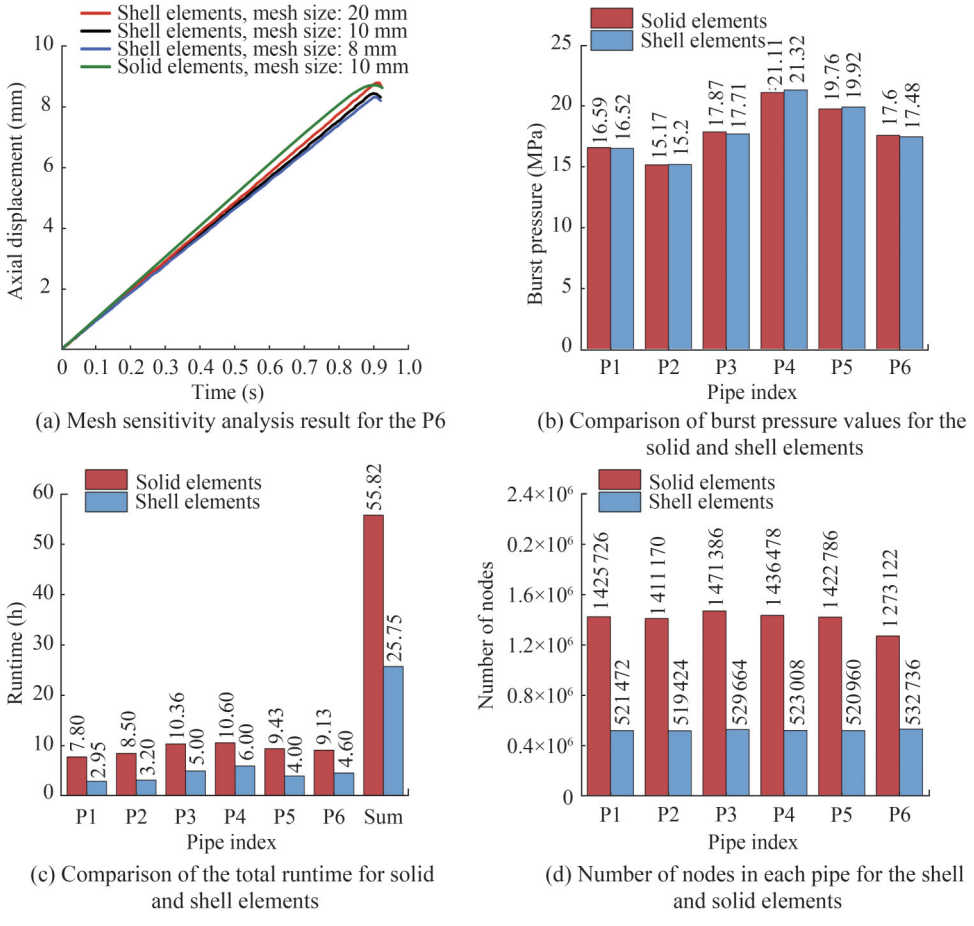


(c) Pressure-increment and increment size-increment graph for the regenerated model, with the black dashed line indicating the instability pressure

Figure 7 Regenerated model results

yielded more accurate predictions since the R^2 values of each ML model in this group were higher than those of Groups 1 and 3, and the difference between the training and test R^2 values was lower than 0.1. The highest differences between the R^2 values for the training and test sets were observed in SVM-3, with a value of 0.14, followed by SVM-1 with a difference of 0.13. Although in most models, the difference between the training and test R^2 values did not exceed 0.1, the R^2 values for the training and test sets were lower than those in Group 2. This phenomenon indicates two important aspects. First, models in which the difference between the R^2 values exceeded 0.1 (SVM-1 and SVM-3) experienced slight overfitting due to the small dataset size and the complexity of inputs in Groups 1 and 3. Second, the lower R^2 values for both the training and test sets observed in the remaining models in Groups 1 and 3 suggest that these models could not learn meaningful patterns from the training set, resulting in poor generalization on the test set. In other words, $N_{defects}$, L_{avg}, and d_{avg} were the suitable features for predicting the burst pressure.

To facilitate a clearer comparison and better understanding of the performance of each model, the predicted – actual graph for all models is shown in Figure 10. The black dashed line represents the ideal fit, where the predicted values exactly match the actual values. The data points closer to this line indicate a robust predictive performance. According to the training results, SVM-2, with an MSE of 0.15 and an R^2 of 0.96, demonstrated acceptable predictive performance. Furthermore, in the test set, SVM-2 achieved the highest R^2 value (0.95) and the lowest MSE (0.19) among all models. Thus, this model is one of the most accurate models in this study. Besides SVM-2, MLP-2 exhibited acceptable predictive performance, with an MSE of 0.09 and an R^2 of 0.98 in the training set and an MSE of 0.31 and an R^2 of 0.92 in the test set. Consequently, among all the models considered in this study, MLP-2 and SVM-2 provided the most accurate predictions.



(a) Mesh sensitivity analysis result for the P6

(b) Comparison of burst pressure values for the solid and shell elements

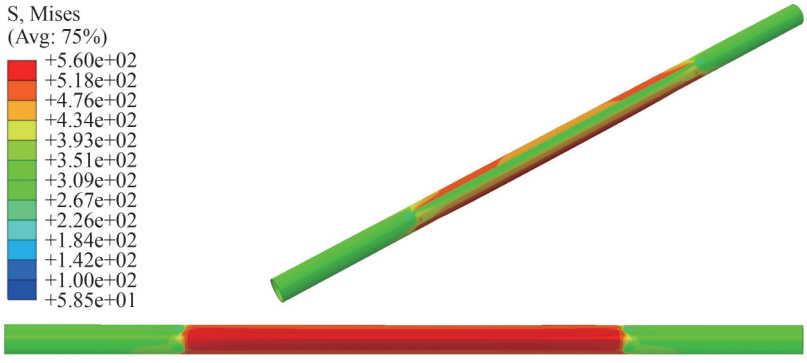
(c) Comparison of the total runtime for solid and shell elements

(d) Number of nodes in each pipe for the shell and solid elements

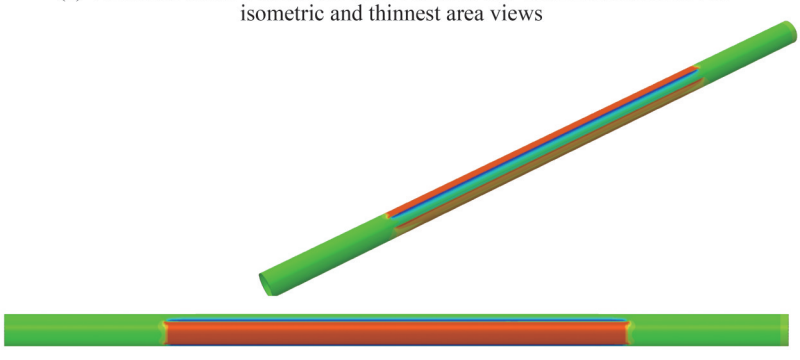
Figure 8 P6 mesh sensitivity and comparison of solid and shell elements models in burst pressure, runtime, and number of nodes

To further evaluate the predictive accuracy, the tolerance graphs for MLP-2 and SVM-2 were plotted (Figure 11). The red dashed line represents the ideal fit, where the predicted burst pressure matches the actual burst pressure perfectly. Additionally, two tolerance areas are shown in Figure 11: in the green areas, the differences between actual and predicted values do not exceed 2.5%, while the yellow areas represent a deviation of up to 5%. The absence of a specific pattern in these graphs indicates that the predictions of both models were unbiased. Although a few data points are outside the yellow areas, most of the predictions are within acceptable error margins. Furthermore, a larger proportion of data points in MLP-2 (Figure 11(a)) are within the yellow areas, while the majority of predictions in SVM-2 (Figure 11(b)) are within the green areas, suggesting that SVM-2 provided more precise predictions. Hence, SVM-2 was considered the most accurate model in this study. Therefore, further investigations on the importance of contributing factors and the effect of input parameters on the burst pressure prediction were conducted exclusively for SVM-2. The standard assessment equations are typically derived by adopting simplifying assumptions. For instance, the DNV-RP-F101 guideline provides a formula applicable only to single, longitudinally oriented, rectangular corrosion defects. Karuppanan et al. (2014) showed that even for isolated corrosion defects, these standard equations often yield conservative results compared to the FEA outcomes. Importantly, the standard equations do not account for the presence of multiple defects or their interaction effects, such as stress concentration zones and nonlinear failure behaviors. These effects significantly limit their applicability in more complex scenarios. Therefore, a direct comparison with standard equations is not applicable in this study because of the presence of multiple defects and the limitations of the equations.

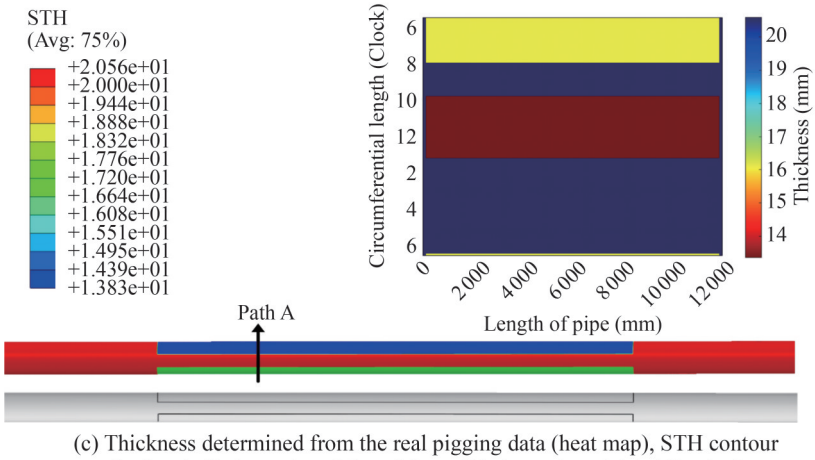
The SHAP analysis, based on game theory (Lundberg et al., 2020), was adopted to analyze the effect of input factors on the predicted burst pressure. The SHAP method quantifies the contribution of each input variable to the final prediction. Figure 12(a) presents the SHAP analysis results for the SVM-2 model, illustrating the effect of all three input variables on the predicted burst pressure of corroded pipes. The SHAP diagram consists of two parts: a scatter graph, where inputs are arranged in the order of the highest to the lowest contribution, and a gradient legend, which visually represents the magnitude and direction of the effect of each input on the output.



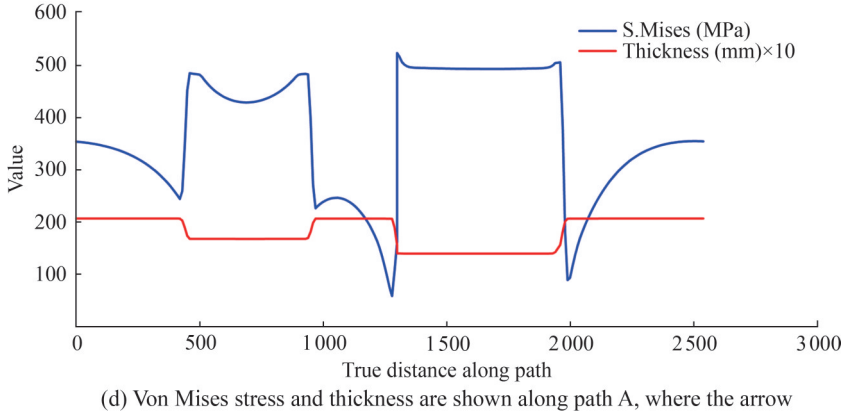
(a) Von mises stress contour for the P6 in the solid element model in both isometric and thinnest area views



(b) Von Mises stress contour for the P6 in the shell element model in both isometric and thinnest area views



(c) Thickness determined from the real pigging data (heat map), STH contour for the shell element model, and the solid element model (white pipe)



(d) Von Mises stress and thickness are shown along path A, where the arrow indicates the direction

Figure 9 P6 results at the time of instability

Table 2 Results of all ML models based on statistical criteria

Model	Training set		Test set	
	MSE	R^2	MSE	R^2
SVM-1	0.25	0.94	0.67	0.81
MLP-1	0.86	0.77	1.12	0.75
GP-1	1.04	0.73	1.27	0.70
SVM-2	0.15	0.96	0.19	0.95
MLP-2	0.09	0.98	0.31	0.92
GP-2	0.49	0.88	0.65	0.83
SVM-3	0.07	0.98	0.5	0.84
MLP-3	0.9	0.76	1.02	0.72
GP-3	0.84	0.77	1.32	0.70

According to Figure 12(b), the most influential factor for predicting burst pressure is the average defect depth (d_{avg}), which contributes 56.21% to the prediction. This is followed by the average defect length (L_{avg}), which contributes 27.51% to the prediction. Furthermore, Figure 12(a) shows that when the color gradient shifts toward red (indicating an increase in these variables), the SHAP value decreases, confirming an inverse correlation among d_{avg}, L_{avg}, and burst pressure. This relationship agrees with the real conditions, as an increase in both the depth and length results in a reduction in pipe thickness, ultimately lowering the burst pressure. The impact of $N_{defects}$ was less clearly defined compared to the other two factors. Its effect is associated with the distribution of defects across the pipe surface. When defects are closely spaced, their

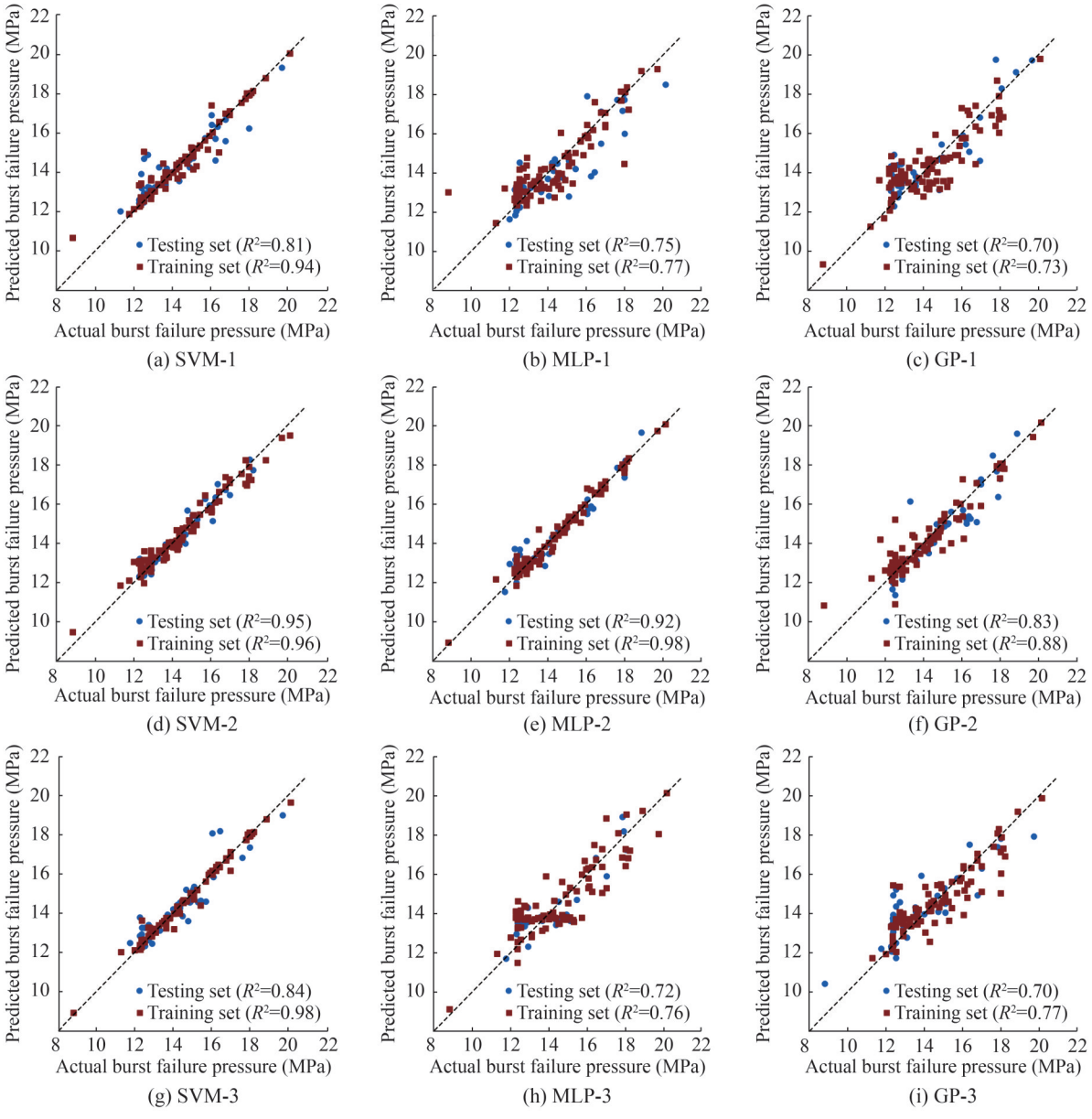
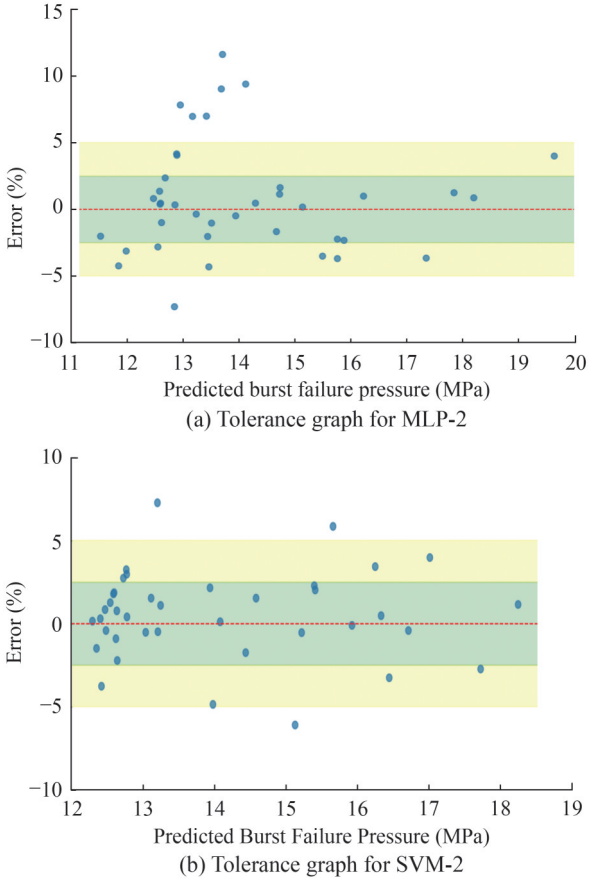


Figure 10 Actual–predicted graph for all ML models

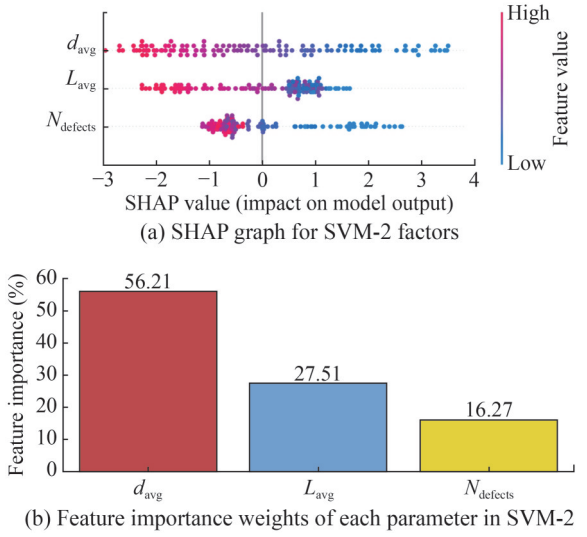


(a) Tolerance graph for MLP-2

(b) Tolerance graph for SVM-2

Figure 11 Tolerance graphs for MLP-2 and SVM-2. The green and yellow areas indicate tolerances of 2.5% and 5%, respectively. The red dashed line represents the ideal fit

cumulative effect results in a lower burst pressure value. Therefore, even when the number of corroded areas in the pipe was relatively low, their proximity led to a cumulative effect, ultimately reducing the burst pressure.



(a) SHAP graph for SVM-2 factors

(b) Feature importance weights of each parameter in SVM-2

Figure 12 SHAP and feature-importance graphs for each parameter in SVM-2

4 Conclusion

This study integrates FEM with ML models to predict the burst pressure in real-world API 5L X65 pipes containing multiple corrosion defects. The FEA employs both solid and shell elements and utilizes the API 579 standard modified by the DNV-RP-F101 (2019) approach to calculate burst pressures. Subsequently, three ML models were developed for three different cases, resulting in a total of nine conditions for burst pressure prediction. The developed models demonstrated good predictive performance within the available dataset. An effective framework was developed by integrating FEA and ML. This framework estimated the burst pressure of corroded pipes. However, there are limitations: for example, the dataset is small (128 samples); a single pipe specification is used (outer diameter of 812.6 mm, API 5L X65); and the simplified defect geometries were derived from pigging data. These factors may restrict the broader applicability of the models. Future work should focus on expanding the dataset and incorporating more accurate inspection data to improve model robustness and generalizability. The main conclusions drawn from this study are as follows:

1) A comparison of the results obtained from the finite element simulations reveals that burst pressure predictions obtained using shell elements are highly consistent with those obtained using solid elements.

2) The shell elements require fewer computational resources, reducing the total runtime to half that of the solid elements, making them a more efficient choice for large-scale analyses.

3) Among all the input configurations, Group 2, which utilized the number of defects, average length of defects, and average depth of defects, achieved the most accurate predictions.

4) Among the evaluated models, MLP-2 and SVM-2 demonstrated comparatively better performance than all the other models. The actual–predicted graphs suggest a potential for generalization to unseen data. However, SVM-2 exhibited more accurate predictions, as most of its predicted values were within the green areas, indicating minimal deviation from the actual values.

5) According to the SHAP graph, the average depth was inversely related to burst pressure and had the highest feature importance weight, indicating its critical role in accurately predicting structural integrity.

Competing interests The authors have no competing interests to declare that are relevant to the content of this article.

Reference

ABAQUS (2022) User Manual

Abyani M, Bahaari MR, Zarrin M, Nasseri M (2022) Predicting

failure pressure of the corroded offshore pipelines using an efficient finite element based algorithm and machine learning techniques. Ocean Engineering 254: 111382. https://doi.org/10.1016/j.oceaneng.2022.111382

Abyani M, Karimi M, Shahgholian-Ghahfarokhi D (2024) Failure assessment of corroded offshore pipelines using code-based approaches and a combination of numerical analysis and artificial neural network. International Journal of Pressure Vessels and Piping 209: 105194. https://doi.org/10.1016/j.ijpvp.2024.105194

Adib-Ramezani H, Jeong J, Pluvinage G (2006) Structural integrity evaluation of X52 gas pipes subjected to external corrosion defects using the SINTAP procedure. International Journal of Pressure Vessels and Piping 83: 420-432. https://doi.org/10.1016/j.ijpvp.2006.02.023

Alang N, Razak N, Shafie KA, Sulaiman A (2013) Finite element analysis on burst pressure of steel pipes with corrosion defects. 13th International Conference on Fracture 2013, ICF 2013 5: 3733-3742

Amaya-Gómez R, Sánchez-Silva M, Bastidas-Arteaga E, Schoefs F, Muñoz F (2019) Reliability assessments of corroded pipelines based on internal pressure-A review. Engineering Failure Analysis 98: 190-214. https://doi.org/10.1016/j.engfailanal.2019.01.064

API 579 (2019) API 579-1/ASME FFS-1: Fitness-For-Service. American Petroleum Institute

Arumugam T, Karuppanan S, Ovinis M (2020) Finite element analyses of corroded pipeline with single defect subjected to internal pressure and axial compressive stress. Marine Structures 72: 102746. https://doi.org/10.1016/j.marstruc.2020.102746

ASME B31G (2012) Manual for Determining the Remaining Strength of Corroded Pipelines

Barbosa AA, Teixeira AP, Soares CG (2017) Strength analysis of corroded pipelines subjected to internal pressure and bending moment. In: Progress in the Analysis and Design of Marine Structures. CRC Press

Benjamin AC, Vieira RD, Freire JLF, de Castro JTP (2000) Burst Tests on Pipeline With Long External Corrosion. In: IPC2000. Volume 2: Integrity and Corrosion; Offshore Issues; Pipeline Automation and Measurement; Rotating Equipment

Beretta S (2021) More than 25 years of extreme value statistics for defects: Fundamentals, historical developments, recent applications. International Journal of Fatigue 151: 106407. https://doi.org/10.1016/j.ijfatigue.2021.106407

Bhardwaj U, Teixeira AP, Guedes Soares C (2022) Probabilistic safety assessment of the burst strength of corroded pipelines of different steel grades with calibrated strength models. Marine Structures 86: 103310. https://doi.org/10.1016/j.marstruc.2022.103310

Bhardwaj U, Teixeira AP, Guedes Soares C (2024) Calibration of burst strength models of corroded pipelines using the hierarchical Bayesian method. Structural Safety 108: 102444. https://doi.org/10.1016/j.strusafe.2024.102444

Cai J, Jiang X, Yang Y, Lodewijks G, Wang M (2022) Data-driven Methods to Predict the Burst Strength of Corroded Line Pipelines Subjected to Internal Pressure. Journal of Marine Science and Application 21: 115-132. https://doi.org/10.1007/s11804-022-00263-0

Chen HF, Shu D (2001) Simplified limit analysis of pipelines with multi-defects. Engineering Structures 23: 207-213. https://doi.org/10.1016/S0141-0296(00)00009-2

Chen Y, Zhang H, Zhang J, Li X, Zhou J (2015) Failure analysis of high strength pipeline with single and multiple corrosions. Materials & Design 67: 552-557. https://doi.org/10.1016/j.matdes.2014.10.088

Choi JB, Goo BK, Kim JC, Kim YJ, Kim WS (2003) Development of limit load solutions for corroded gas pipelines. International Journal of Pressure Vessels and Piping 80: 121-128. https://doi.org/10.1016/S0308-0161(03)00005-X

Cronin DS, Pick RJ (2002) Prediction of the failure pressure for complex corrosion defects. International Journal of Pressure Vessels and Piping 79: 279-287. https://doi.org/10.1016/S0308-0161(02)00020-0

Cronin DS, Pick RJ (2000) Experimental Database for Corroded Pipe: Evaluation of RSTRENG and B31G. In: IPC2000. Volume 2: Integrity and Corrosion; Offshore Issues; Pipeline Automation and Measurement; Rotating Equipment

Cronin DS, Roberts KA, Pick RJ (1996) Assessment of Long Corrosion Grooves in Line Pipe. In: IPC1996. Volume 1: Regulations, Codes, and Standards; Current Issues; Materials; Corrosion and Integrity, pp 401-408

DNV-RP-F101 (2019) Corroded pipelines

DNV-ST-F101 (2017) Submarine pipeline systems

Du X, Zhang J, Peng H, Liu Y (2017) Plastic Limit Analysis of Modified 9Cr-1Mo Steel Pressure Vessel Containing Volume Defect with Creep Damage Law. Int J Appl Mechanics 09: 1750025. https://doi.org/10.1142/S1758825117500259

Fallqvist B (2009) Collapse of thick deepwater pipelines due to hydrostatic pressure

Freire JLF, Vieira RD, Castro JTP, Benjamin AC (2006) Part 3: Burst tests of pipeline with extensive longitudinal metal loss. Experimental Techniques 30: 60-65. https://doi.org/10.1111/j.1747-1567.2006.00109.x

Gao S, Shao N, Yang L (2010) Determining the Remaining Strength of Corroded Pipelines with B31G Code and Finite Element Analysis Theory. In: 2010 International Conference on Measuring Technology and Mechatronics Automation. pp 1097-1100

Ghari H, Taherizadeh A, Sadeghian B, Sadeghi B, Cavaliere P (2024) Metallurgical characteristics of aluminum-steel joints manufactured by rotary friction welding: A review and statistical analysis. Journal of Materials Research and Technology 30: 2520-2550. https://doi.org/10.1016/j.jmrt.2024.03.089

Han S, Qubo C, Meng H (2012) Parameter selection in SVM with RBF kernel function. In: World Automation Congress 2012. pp 1-4

Hasni H, Alavi AH, Jiao P, Lajnef N (2017) Detection of fatigue cracking in steel bridge girders: A support vector machine approach. Archives of Civil and Mechanical Engineering 17: 609-622. https://doi.org/10.1016/j.acme.2016.11.005

Jiang F, Dong S (2024) Development of an integrated deep learning-based remaining strength assessment model for pipelines with random corrosion defects subjected to internal pressures. Marine Structures 96: 103637. https://doi.org/10.1016/j.marstruc.2024.103637

Karuppanan S, Wahab AA, Patil S, Zahari MA (2014) Estimation of Burst Pressure of Corroded Pipeline Using Finite Element Analysis (FEA). Advanced Materials Research 879: 191-198. https://doi.org/10.4028/www.scientific.net/AMR.879.191

Koch G, Varney J, Thompson N, Moghissi O, Gould M, Payer J (2016) International Measures of Prevention, Application, and Economics of Corrosion Technologies Study. NACE International

Liu X, Xia M, Bolati D, Liu J, Zheng Q, Zhang H (2020) An ANN-based failure pressure prediction method for buried high-strength pipes with stray current corrosion defect. Energy Science & Engineering 8: 248-259. https://doi.org/10.1002/ese3.522

Lundberg SM, Erion G, Chen H, DeGrave A, Prutkin JM, Nair B, Katz R, Himmelfarb J, Bansal N, Lee S-I (2020) From local explanations to global understanding with explainable AI for

trees. Nat Mach Intell 2: 56-67. https://doi. org/10.1038/s42256-019-0138-9

Luo Q, Yin L, Simpson TW, Beese AM (2022) Effect of processing parameters on pore structures, grain features, and mechanical properties in Ti-6Al-4V by laser powder bed fusion. Additive Manufacturing 56: 102915. https://doi.org/10.1016/j.addma.2022.102915

Ma B, Shuai J, Liu D, Xu K (2013) Assessment on failure pressure of high strength pipeline with corrosion defects. Engineering Failure Analysis 32: 209-219. https://doi.org/10.1016/j.engfailanal.2013.03.015

Mok DHB, Pick RJ, Glover AG, Hoff R (1991) Bursting of line pipe with long external corrosion. International Journal of Pressure Vessels and Piping 46: 195-216. https://doi.org/10.1016/0308-0161(91)90015-T

Mokhtari M, Melchers RE (2018) A new approach to assess the remaining strength of corroded steel pipes. Engineering Failure Analysis 93: 144-156. https://doi.org/10.1016/j.engfailanal.2018.07.011

Mucek MW (1999) Detection, Repair, and Mitigation of Wet H2S Cracking: An Overview of RP0296. OnePetro

Netto TA, Ferraz US, Estefen SF (2005) The effect of corrosion defects on the burst pressure of pipelines. Journal of Constructional Steel Research 61: 1185-1204. https://doi.org/10.1016/j.jcsr.2005.02.010

Neural network models (supervised) Scikit-learn Documentation. In: scikit-learn. https://scikit-learn/stable/modules/neural_networks_supervised.html

Poorhaydari K (2019) Failure of a hydrogenerator reactor inlet piping by high-temperature hydrogen attack. Engineering Failure Analysis 105: 321-336. https://doi. org/10.1016/j. engfailanal. 2019.07.003

Rasamoelina AD, Adjailia F, Sinčák P (2020) A Review of Activation Function for Artificial Neural Network. In: 2020 IEEE 18 th World Symposium on Applied Machine Intelligence and Informatics (SAMI). pp 281-286

RBF SVM parameters Scikit-learn Documentation. https://scikit-learn/stable/auto_examples/svm/plot_rbf_parameters.html

Shuai Y, Shuai J, Xu K (2017) Probabilistic analysis of corroded pipelines based on a new failure pressure model. Engineering Failure Analysis 81: 216-233. https://doi.org/10.1016/j.engfailanal.2017.06.050

Stephens DR, Leis BN (2016) Development of an Alternative Criterion for Residual Strength of Corrosion Defects in Moderate- to High-Toughness Pipe. American Society of Mechanical Engineers Digital Collection

Sun J, Cheng YF (2018) Assessment by finite element modeling of the interaction of multiple corrosion defects and the effect on failure pressure of corroded pipelines. Engineering Structures 165: 278-286. https://doi.org/10.1016/j.engstruct.2018.03.040

Wang H, Fang X, Liu G, Xie Y, Tian X, Leng D, Mu W (2021) An Approach to Predicting Fatigue Crack Growth Under Mixed-Mode Loading Based on Improved Gaussian Process. IEEE Access 9: 48777-48792. https://doi.org/10.1109/ACCESS.2021.3050132

Webster S, Bannister A (2000) Structural integrity assessment procedure for Europe – of the SINTAP programme overview. Engineering Fracture Mechanics 67: 481-514. https://doi.org/10.1016/S0013-7944(00)00070-9

Xing J, Zayed T, Ma S (2024) Corrosion-based failure analysis of steel saltwater pipes: A Hong Kong case study. Engineering Failure Analysis 161: 108266. https://doi.org/10.1016/j.engfailanal.2024.108266

Yamaguchi A (2014) Investigation of Burst Pressure in Pipes With Square Wall Thinning by Using FEA and API579 FFS-1. American Society of Mechanical Engineers Digital Collection

Yu W, Vargas PM, Karr DG (2011) Bending Capacity Analyses of Corroded Pipeline. Journal of Offshore Mechanics and Arctic Engineering 134: https://doi.org/10.1115/1.4004521

Zangeneh S (2021) Fitness-For-Service Assessment and Failure Analysis of Hydrogen-Induced Cracking in a Pipeline Steel. J Fail Anal and Preven 21: 1875-1887. https://doi.org/10.1007/s11668-021-01248-x

Zhang Y, Yang L, Fang H, Ma Y, Ning B (2024) Assessment for burst failure of subsea production pipeline systems based on machine learning. Ocean Engineering 304: 117873. https://doi. org/10.1016/j.oceaneng.2024.117873

Zhou R, Gu X, Bi S, Wang J (2022) Finite element analysis of the failure of high-strength steel pipelines containing group corrosion defects. Engineering Failure Analysis 136: 106203. https://doi.org/10.1016/j.engfailanal.2022.106203

Zhu XK, Leis BN (2005) Influence of Yield-to-Tensile Strength Ratio on Failure Assessment of Corroded Pipelines. Journal of Pressure Vessel Technology 127: 436-442. https://doi.org/10.1115/1.2042481

Zvirko O, Nykyforchyn H, Krechkovska H, Tsyrulnyk O, Hredil M, Venhryniuk O, Tsybailo I (2024) Evaluating hydrogen embrittlement susceptibility of operated natural gas pipeline steel intended for hydrogen service. Engineering Failure Analysis 163: 108472. https://doi.org/10.1016/j.engfailanal.2024.108472